Research Article

Isotope and hydrochemical characteristics of thermal waters along the active fault zone (Erzin-Hatay/Türkiye) and their geothermal potential

Didem YASİN[1,*] , **Galip YÜCE**[2]

[1]Department of Geological Engineering, Eskişehir Osmangazi University, , Eskişehir, Turkiye
[2]Department of Geological Engineering, Hacettepe University, , Beytepe, Ankara, Turkiye

Abstract: Geochemical investigations carried out on thermal waters over the Erzin-Hatay area allowed the collection of a suite of 9 samples from natural springs and one well characterized by outlet temperatures in the range from 19.6 to 31.5 °C. All of the springs have slightly acidic pH (in the range of 6) but one sample was marked by a pH value >11 as a consequence of serpentinization processes. The water chemistry denotes water/rock interactions with either magmatic or carbonatic rocks in a water reservoir equilibrated at temperatures estimated to be in the range of 58–162 °C. The stable isotope composition of the collected waters, in terms of dD and $d^{18}O$, denotes a recharge from local meteoric waters. The dissolved gases denote the contribution of no atmospheric components. CO_2 is the dominant dissolved component for most of the sample, while methane is the major component for the thermal water involved in serpentinization. Besides the main components CO_2 and CH_4, the dissolved gases show significant concentrations of He, H_2, and CO. The isotopic composition of helium shows $^3He/^4He$ ratios well above that of Air Saturated Waters (ASW = 1.39×10^{-6}) clearly indicating a significant contribution of ^3He of mantle origin. Taking into account the location of some sampling sites nearby the Düziçi-İskenderun Active Fault Zone and the associated mantle helium contribution, we propose that fluids/faults relationships have to be considered as responsible for the feeding of deep-originated fluids to the shallow groundwater. As mantle-derived fluids are also carriers of thermal energy, the collected results strongly suggest improving the knowledge of the study area, where hydrological and geochemical considerations coupled with the tectonic setting of the area should focus on the geothermal potential of the circulating waters.

Key words: Erzin (Hatay, Türkiye), hydrogeochemistry, fluids geochemistry, geothermometers, active fault and gas relations, origin of methane

1. Introduction

Recent investigations carried out over a volcano-tectonic active area in Eastern Turkey highlighted the presence of circulating thermal waters marked by typical mantle or magma-derived geochemical features (Yuce et al., 2014). The increased need for energy is pushing humankind to look for new energy sources that have to be clean, renewable, and sustainable. The geothermal energy is a serious perspective due to the infinitive source of heat generated by our planet. The exploitation of such a source is only poorly developed as well as the knowledge of the processes occurring behind the thermal energy transfer from the deep mantle to the shallow levels. The evidence of a widespread presence of thermal manifestations over the Erzin-Hatay area is an indication of the probable existence of geothermal reservoirs. The area is crossed by active faults and exhibits outcrops of recent volcanic rocks.

The research area, in fact, is located close to the boundary of three main tectonic plates, namely, Anatolian, African, and Arabian plates. Geological units in the study area, from the oldest to the youngest consist of pre-Jurassic metamorphic, Cretaceous aged ophiolite complex, Mesozoic limestone-dolomite, Neogene aged clastic (sandstone and conglomerate) and carbonate rocks, Plio-Quaternary and Ouaternary basalt, and alluvial sediments in Quaternary aged (Figure 1). The Erzin ophiolite is a remnant of the oceanic lithosphere and is part of a peri-Arabian ophiolite belt that includes the Troodos (Cyprus), Baër- Bassit (Syria) and Semail (Oman) ophiolites in the Eastern Mediterranean Region (Dilek and Thy, 2009) which genetically and tectonically belong to the Southern Tethys (Şengör and Yılmaz, 1981). Furthermore, Erzin Province is a strong earthquake-prone area due to the active fault segments of the East Anatolian Fault. That segment is the major strike-slip fault zone in Eastern Turkey, namely İskenderun-Düziçi Fault (IDF) and Toprakkale Fault (TF) crossing over the area (Figure 1).
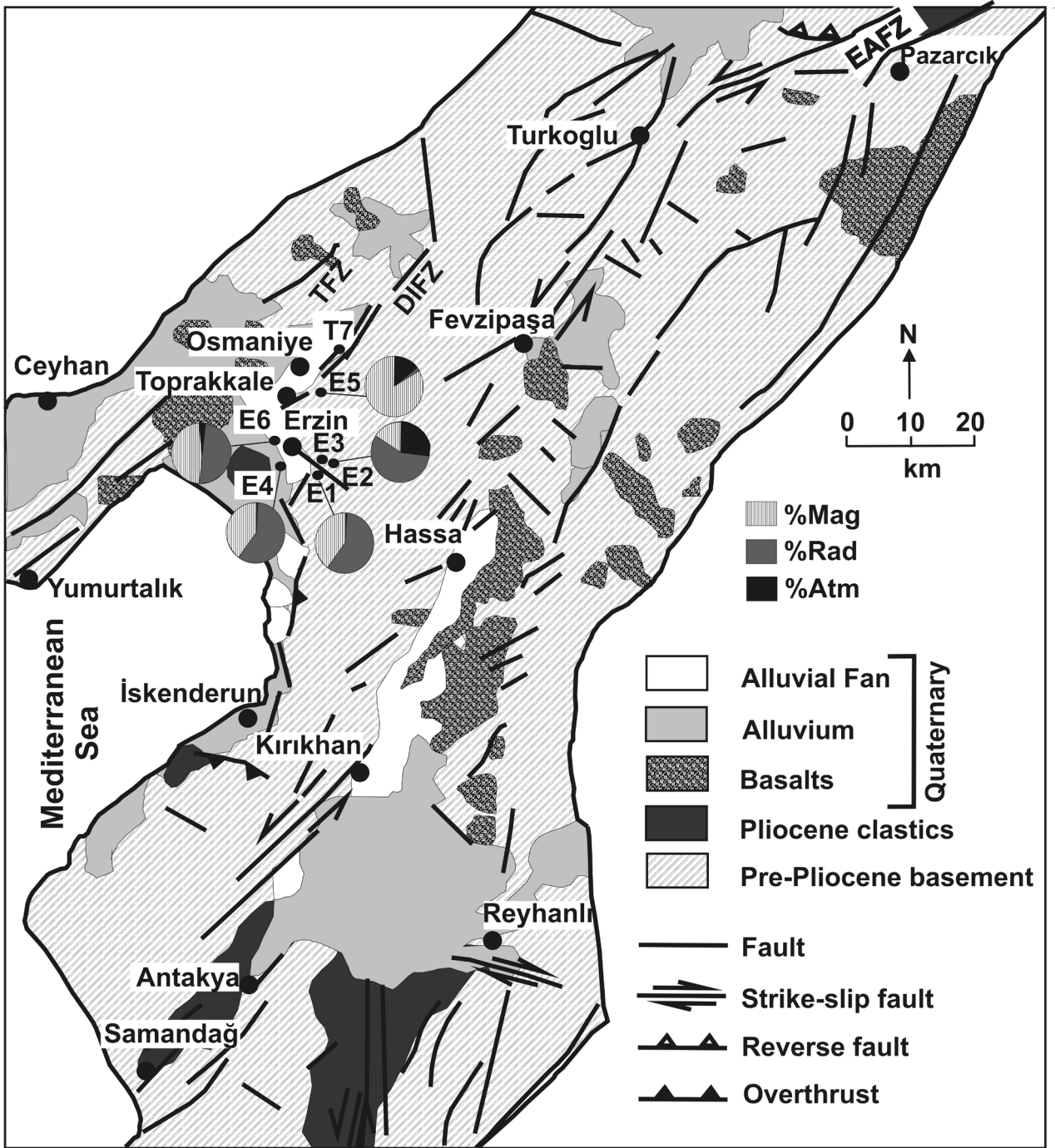
* Correspondence: dugurlu@ogu.edu.tr

Figure 1. Geological map of the Erzin Province (modified from Rojay et al. 2001) and locations of water sampling points (DİFZ: Düziçi–İskenderun Fault Zone, KFS: Karataş Fault Segment, YFS: Yumurtalık Fault Segment, TFS: Toprakkale Fault Segment, AFS: Amanos Fault Segment, YEFS: Yesemek Fault Segment, NFZ: Narlı Fault Zone (modified from Duman et al. 2020). Pie (circle) charts shown in the different pattern fill or color refer to the proportional ratio of atmospheric, crustal, and mantle Helium contributions.

Despite several geological, tectonic and hydrogeological studies were carried out over the region (Dewey et al., 1973; Perinçek and Çemen, 1990; Rojay et al., 2001; Tatar et al., 2004; Karabacak, 2007; Altunel et al., 2009; Karabacak et al., 2010; Italiano et al., 2017; Yuce et al., 2017; D'Alessandro et al., 2018; Duman et al., 2020; Şener et al., 2021), none of them focused on the fluids/fault interactions as well as on the geochemistry of thermal waters vented over the rea.

This paper accounts for the geochemical features of water samples collected over a ~500km²-wide area as well as their potential as geothermal energy carriers. The geochemical results also allow for constraining the relationships of the circulating fluids with the fault segments recognized as active, seismogenic faults (Figure 1).

2. Materials and methods

Nine samples were taken from the six locations between 2013 and 2014 (Figure 1 and Table 1). The samples were collected from five natural springs and one 600m-deep borehole at artesian flow conditions with a flow rate of 5–6 L/s, drilled by the MTA (General Directorate of Mineral Research and Exploration of Turkey).

Electrical Conductivity (EC), temperature (°C), pH, and Eh values were measured on-site using a YS-556 model multi-parameter instrument. On the field, the water samples for cation analyses were filtered with 0.45-μm filter paper. Samples for cation analyses were also acidified to pH ≤ 2 by adding 0.5 N nitric acid. Samples for environmental isotopes (oxygen-18, deuterium, and tritium) were collected without any treatment.

Some samples have also been collected for the chemical and isotopic analyses of the dissolved gas phase. They were sealed underwater in 240 mL pyrex vials using silicon/teflon septa and purpose-built pliers, following the methodology and instrumentation described in Italiano et al., (2009).

The samples had been delivered to the laboratory by express courier in order to perform the analytical processes within two-three weeks after sampling (Italiano et al., 2014).

The geochemical determinations of major ions, dissolved gas composition, and stable and noble gas isotopic ratios were performed at the INGV (National Institute of Geophysics and Volcanology) laboratories of Palermo, Italy, while tritium contents were determined at the Hacettepe University laboratory in Turkey.

2.1. Analytical methods

In the laboratory, the chemical composition was determined by high-pressure liquid chromatography (HPLC Dionex 2001) using a Dionex CS-12 and a Dionex AS4A-SC column for cations and anions determinations, respectively. Typical uncertainties were within ±5%.

The dissolved gases were extracted after equilibrium was reached at a constant temperature with a host-gas (high-purity argon) injected in the sample bottle (for further details see Italiano et al., 2009, 2013). Chemical analyses of gas species were carried out by gas chromatography (Perkin Elmer Clarus500 equipped with a double TCD-FID detector) using argon as the carrier gas. Typical uncertainties were within ±2%.

Silica content was performed by Hach Lange DR6000 using 4500 SiO_2 Molybdosilicate standard method in error limits within ±7.8%.

The stable isotope composition ($\delta^{18}O$ and δD) of water samples was acquired using mass-spectrometry and expressed in δ‰ with respect to the international standard V-SMOW (Vienna Standard Mean Ocean Water). The error limits are ±0.1‰ and ±1‰ for $\delta^{18}O$ and δD, respectively.

The tritium contents are determined by electrolytic enrichment and liquid scintillation spectrometry. The results are given as Tritium Units (TU) with an analytical error of 0.3 TU.

Table 1. List of the sample locations together with the T (°C), pH, electrical conductivity (in mS/cm), and oxidation-reduction potential (in mV). Coordinates in UTM-WGS84

Sample No	Site name	Easting	Northing	Altitude (m)	Date	T (°C)	pH	Eh (mV)	EC (µmho/cm)
E1-1	Erzin MTA thermal well	36.950629	36.250209	340	18.01.2013	27	6.00	n.d.	n.d.
E1-2					26.06.2013	27.2	6.28	−80	4639
E1-3					18.09.2014	27.2	6.30	−98	5029
E2	Erzin spring water	36.960100	36.265600	480	26.06.2013	31.5	6.38	−80	5275
E3	Erzin spring water	36.959960	36.267270	460	26.06.2013	22.0	6.33	−63.4	3340
E4-1	Kokarca spring water	36.958150	36.211826	200	26.06.2013	19.3	6.15	−211	2513
E4-2					18.09.2014	19.6	6.00	−210	2863
E5	Osmaniye (Gebeli) spring water	37.069400	36.294800	300	26.06.2013	21.3	6.18	88.7	1591
E6	Gokdere spring water	37.006349	36.200964	265	18.09.2014	23.3	11.40	−275	7483

The isotope composition of dissolved He was analyzed on gas fractions extracted by headspace equilibration and purified following methods described in the literature (Yuce et al., 2014 and references therein). The isotopic analyses of the purified helium fraction were performed using a static vacuum mass spectrometer (GVI5400TFT) that allows the simultaneous detection of ^{3}He and ^{4}He ion beams, thereby keeping the ^{3}He/^{4}He error of measurement to very low values. Typical uncertainties in the range of low-^{3}He samples are within ±2%.

The isotope composition of He is expressed by R/R$_a$ which refers ^{3}He/^{4}He of the sample versus the atmospheric ^{3}He/^{4}He (R$_a$ = 1.386 × 10^{-6}). Analytical results of He isotopes were corrected for the atmospheric contamination of the sample (R$_c$/R$_a$) on the basis of its ^{4}He/^{20}Ne ratio (Sano and Wakita, 1988).

3. Results

The in situ measurements and analytical results of water chemistry, environmental isotopes, composition of dissolved gas, and estimated reservoir temperatures are given in Tables 2–5, respectively. The multinotation of sampling codes refers to different sampling dates from the same sampling location, such as E1-1, E1-2, and E1-3.

3.1. Hydrochemical features

EC, pH, and temperature of samples ranged from 1591 to 7483 µmho/cm, 6 to 11.4 and 19.3 °C to 31.5 °C respectively (Table 1). EC in mS/cm; Eh in mV. A typical composition of the Mediterranean Sea water is reported for comparison. All the thermal waters display negative Eh values but the sample from Osmaniye is marked by positive values. That sample exhibit also has the lowest EC value.
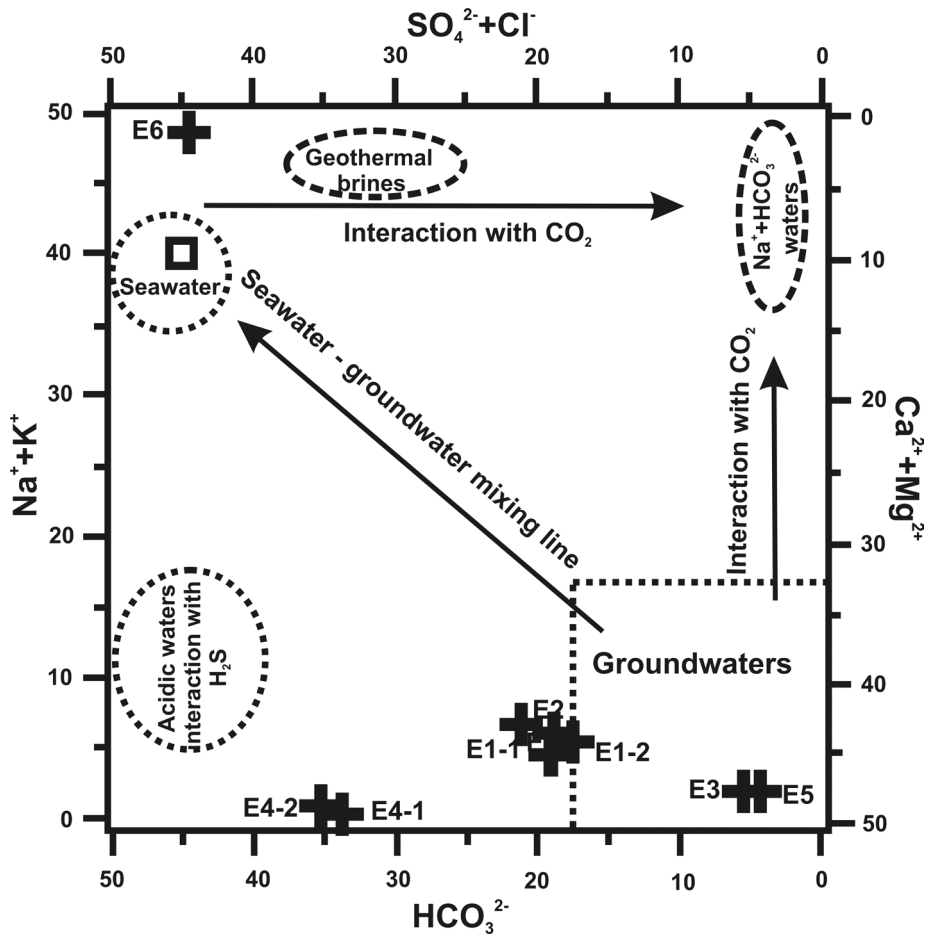

Figure 2. Langelier-Ludwig plot showing how the collected thermal waters fall in the field of groundwaters. The reported typical fields and interactions lines highlight the occurrence of gas/water interaction processes and rules out mixings with seawater or geothermal brines for sample E6.

The major ions show concentration ranges very different for the different samples (Table 2). Na content is relatively high in sample E6 (Gökdere) with respect to the other waters where it ranges from 0.16 meq/L in E4 to about 6 in E1 and slightly above 10 in E2. Contrastingly, Mg content is very low (below the detection limits) for E6 while it is in the range of 45 meq/L for samples E1, E2, and E3 and around 14 meq/L for samples E4 and E5. Calcium shows a similar behavior with very low concentration for sample E6 (1.9 meq/L) and higher concentrations for all the other samples.

The anions show similar trends as for the cations: sample E6 has the highest Cl content (54.3meq/L) compared to a range from 0.2 (E4) to 5.3 (E2) for the other samples. In contrast, sample E6 shows the lowest HCO_3 content (6.3 meq/L). The bicarbonates vary in a range from 12.5 (E4) to 55.3 (E2).

3.2. Isotopic composition of waters
The results of isotopic analyses of the water samples are given in Table 3. The $d^{18}O$ isotope ratio ranges from –6.52‰ to –4.26‰ for $d^{18}O$ and from –35.00‰ to –24.30‰ dD.

Tritium content is in the range of 0.5TU for samples E1-E2, and 3.5TU for samples E4 and E6. Sample E5 shows the highest value of 5.7TU.

3.3. Dissolved gases
Starting from the gas-chromatographic analyses, the composition of the dissolved gas phase was calculated by combining the solubility coefficients (Bunsen coefficient "b", mL_{gas}/L_{H2O}) of each gas species at the equilibration temperature, the volume of gas extracted (mL) the volume of the water sample as shown in equation (1):

$$G_C = \{[G_{gc}] * Vg_e + ([G_{gc}] * b_G * VW)\}VW^{-1} * Vg_e * Vg_i^{-1}/100 \quad (1)$$

where G_C is the concentration of the selected gas specie, G_{gc} is its concentration measured by gas chromatography (vol%), Vg_e and Vg_i represent the extracted and the introduced gas volumes, respectively, while VW is the volume of the analyzed water sample (see also Italiano et al., 2009 and 2013 for further details). All volumes are carefully measured at the equilibration temperature, then the results are converted from cc STP/L to ppm by volume.

The analytical results of Table 4 show the presence of variable oxygen amounts in all the thermal waters. This is a common feature in dissolved gases due to the mixing of the atmospheric component with gases of different origins. The most abundant nonatmospheric component is CO_2 besides variable contents of CH_4, CO, He, and hydrogen in all the samples. In particular, while the dissolved gases for samples E1, 2, and 3 are CO_2-dominated, samples E4 and E5 are N_2-dominated and the gas dissolved in Gökdere (E6) is clearly a CH_4-dominated gas.

4. Discussion
4.1. Waters geochemistry
The very high pH value measured in sample E6 is associated to the absence of magnesium and sulfate as a consequence of serpentinization processes (D'Alessandro et al., 2018). Serpentinites are formed by the aqueous alteration and hydration of ultramafic rocks, which are predominantly composed of olivine and pyroxene minerals.
Following the chemical reaction:

$$(Mg\ Fe)_2\ SiO_4 + H_2O \rightarrow Mg_3Si_2O_5\ (OH)_4 + Mg\ (OH)_2 + Fe_3O_4 + H_2 \quad (2)$$
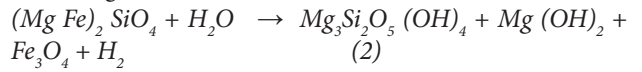
olivine + water → serpentine + brucite + magnetite + hydrogen

the hydrolysis of olivine produces molecular hydrogen (H_2) as a result of the oxidation of ferrous iron (Fe(II)) and the reduction of water. Concordantly, Mg content is totally exploited which is consistent with the high pH and the hydrogen content (see Table 2 and Table 4) of E6.

The Langelier-Ludwig plot of Figure 2 shows how the samples fall in the field of groundwaters but sample E6 falls close to the corner of the halite-sulphate waters. The very low sulphates and calcium contents, however, exclude interaction with selenitic rocks. Moreover, the absence of magnesium ruling out any seawater contamination confirms that the spring in Gökdere represents the venting of hyperalkaline waters due to ongoing serpentinization processes.

4.2. Water/rock interactions
The saturation indices (SI = the degree of saturation of minerals in aqueous solutions with respect to given minerals) were calculated by using the WATSPEC (Wigley, 1977) computer program with respect to water compositions. The results show that all waters are undersaturated with anhydrite and gypsum. E1-1, E1-2, E1-3, and E6 samples are oversaturated with respect to aragonite. Most of the waters are slightly supersaturated in regard to calcite and dolomite.

To check into details of Water/rock Interactions (WRI) with those carbonatic rocks, the Chlorine Alkaline Indices (CAI-1 and CAI-II; Schoeller 1977) were computed using equations (3) and (4).

Those indices account for the ion exchange (concentrations in meq/L) between groundwater and host rocks (Marghade et al. 2012; Li et al. 2012). The positive CAIs (CAI-I) indicate the exchange of Na^+ and K^+ of the water with Mg^{2+} and Ca^{2+} of the rock while negative CAIs (CAI-II) show an opposite exchange between water and rock (Schoeller, 1977; Nagaraju et al., 2006; Thakur et al., 2016; Mahmoudi et al., 2017; Agyemang, 2020).

$$CAI-I = (Cl^- - (Na^+ + K^+))/Cl^- \quad (3)$$

$$CAI-II = \frac{Cl^- - (Na^+ + K^+)}{HCO3^- + SO4^{2-} + CO3^{2-} + NO3^-} \quad (4)$$

Table 2. Chemical composition of the collected thermal waters.

Parameters	Units	E1-1	E1-2	E1-3	E2	E3	E4-1	E4-2	E5	E6	Seawater
		Erzin MTA well			Erzin springs		Kokarca spring		Osmaniye spring	Gokdere spring	
Date		18.01.2013	26.06.2013	18.09.2014	26.06.2013	26.06.2013	26.06.2013	18.09.2014	26.06.2013	18.09.2014	
T	°C	27	27.2	27.2	31.5	22	19.3	19.6	21.3	23.3	n.d.
pH		6	6.28	6.3	6.38	6.33	6.15	6	6.18	11.4	n.d.
Eh	mV	n.d.	−80	−98	−80	−63.4	−211	−210	88.7	−275	n.d.
EC	µhos. 25 °C	n.d.	4639	5029	5275	3340	2513	2863	1591	7483	55500*
Na^+	mg/L	142.00	144.00	148.00	247.00	42.40	3.72	7.50	15.60	1353.00	12,426.00
	meq/L	6.17	6.26	6.43	10.76	1.84	0.16	0.33	0.68	58.83	540.73
K^+	mg/L	24.40	24.2	25.80	39.90	7.40	0.82	1.56	0.57	69.01	456
	meq/L	0.63	0.62	0.66	1.02	0.19	0.02	0.04	0.01	1.77	11.6
Ca^{2+}	mg/L	392.00	473.00	493.00	705.00	172.00	561.00	548.50	169.00	57.70	474
	meq/L	13.07	15.71	16.3	35.3	5.73	28.05	27.43	5.63	2.89	23.66
Mg^{2+}	mg/L	571.00	597.00	552.00	542.00	573.00	183.00	167.10	173.00	0.00	1409
	meq/L	47.58	49.75	46	45.2	47.75	15.25	13.92	14.42	0	115.95
Cl^-	mg/L	117	116	131	191	49.1	7.1	12.6	19.9	1903	21576
	meq/L	3.34	3.31	3.74	5.38	1.4	0.2	0.35	0.56	53.6	607.77
SO_4^{2-}	mg/L	1076.00	1211.00	1023.00	1695.00	219.00	1287.00	1408.00	81.3	5.76	3065.00
	meq/L	22.42	25.23	21.31	35.3	4.56	26.81	29.33	1.69	0.12	63.86
CO_3^{2-}	mg/L	0.00	0.00	0.00	0.00	0.00	0.00	0.00	0.00	0.00	0,00
	meq/L	0.00	0.00	0.00	0.00	0.00	0.00	0.00	0.00	0.00	0,00
HCO_3^-	mg/L	2928.00	2891.00	2902.00	3373.00	3142.00	763.00	781.00	1226.00	390.00	26.00
	meq/L	48.01	47.04	47.58	55.3	51.52	12.51	12.81	20.1	6.39	1.3
B	mg/L	3.412	3.634	n.d.	5.337	1.16	0.126	0.128	0.051	1.002	n.d.
Fe	mg/L	6.19	6.4	n.d.	10.35	3.9	0.35	0.09	0.06	0.0001	n.d.
Mn	mg/L	0.36	0.34	n.d.	0.51	0.45	0.09	0.09	0.06	0.00	n.d.
As	mg/l	22.1	28.1	n.d.	10.98	1.72	129	169	0.06	0.57	n.d.
Br	mg/l	488	n.d.	n.d.	713	134	42.6	n.d.	42.4	n.d.	n.d.
Sr	mg/L	8.75	8.79	n.d.	13.63	1.93	9.28	9.66	0.73	3.53	n.d.
SiO_2	mg/L	144	135.5	141	152.1	118.4	40.5	37.7	65.2	1.9	n.d.
	EN %	4.475	4.28	2.2	1.96	1.7	4.7	0.97	3.7	2.7	
	Water type	$MgHCO_3$	$MgHCO_3$	$MgHCO_3$	Mg, Ca, HCO_3, SO_4	$MgHCO_3$	$CaSO_4$	$CaSO_4$	$MgHCO_3$	NaCl	NaCl

The CAI-I and CAI-II plots of Figure 3a and Figure 3b show negative ratios in terms of the CAIs for most of the samples as a consequence of exchanges of Mg^{2+} and Ca^{2+} of the water with Na^+ and K^+ of the rocks.

Ca^{2+}/Mg^{2+} molar ratio allows to constrain weathering process of carbonate minerals: for Ca^{2+}/Mg^{2+} ratios ≤ 1 dolomite dissolution occurs; for Ca^{2+}/Mg^{2+} ratio from 1 to 2 calcite dissolution is the dominant dissolution process (Mayo and Loucks, 1995). Ca^{2+}/Mg^{2+} ratios higher than 2

indicate silicate dissolution, also providing magnesium and calcium to the groundwater (Mayo and Loucks, 1995; Katz et al., 1997; Lakshmanan et al., 2003; Narany et al., 2014; Mezga and Urbanc, 2014, Setiawan et al., 2020). Overall, the Ca^{2+}/Mg^{2+} ratios of our samples vary from 0.12 to 1.22. Dissolution of dolomite looks to occur for samples E1, E3, and E5, while for sample E4 calcite dissolution seems to be the probable origin of Ca^{2+} and Mg^{2+} ions (Figure 4).
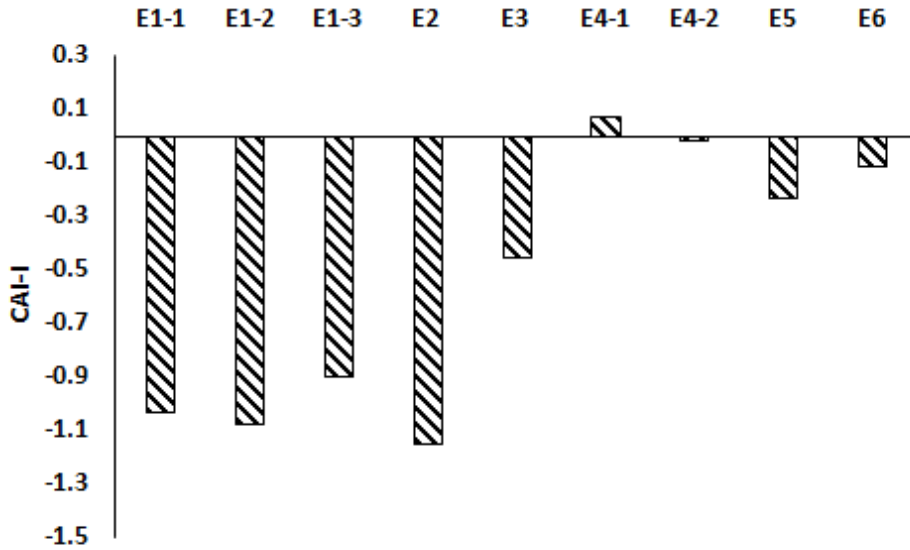
Figure 3a. Bar diagram of CAI-I.
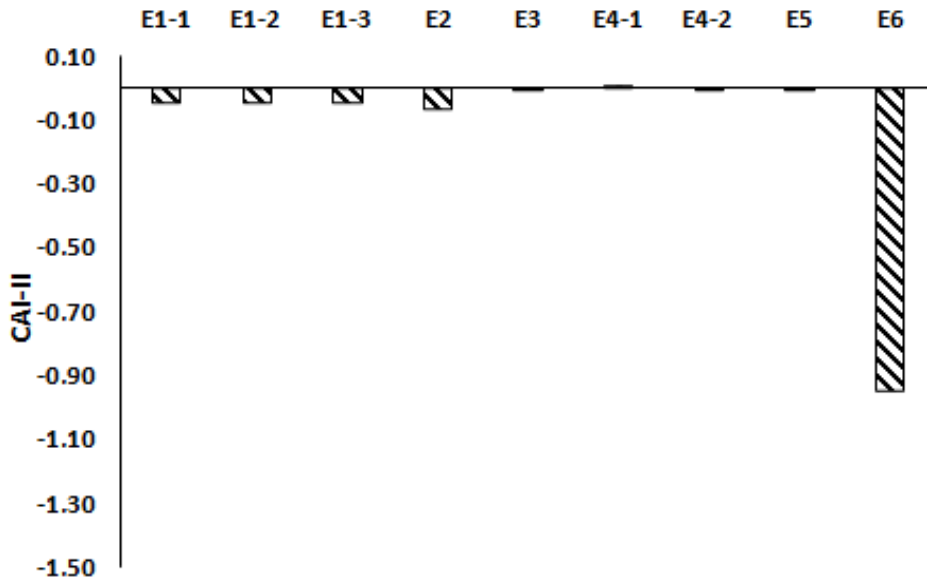
Figure 3b. Bar diagram of CAI-II.
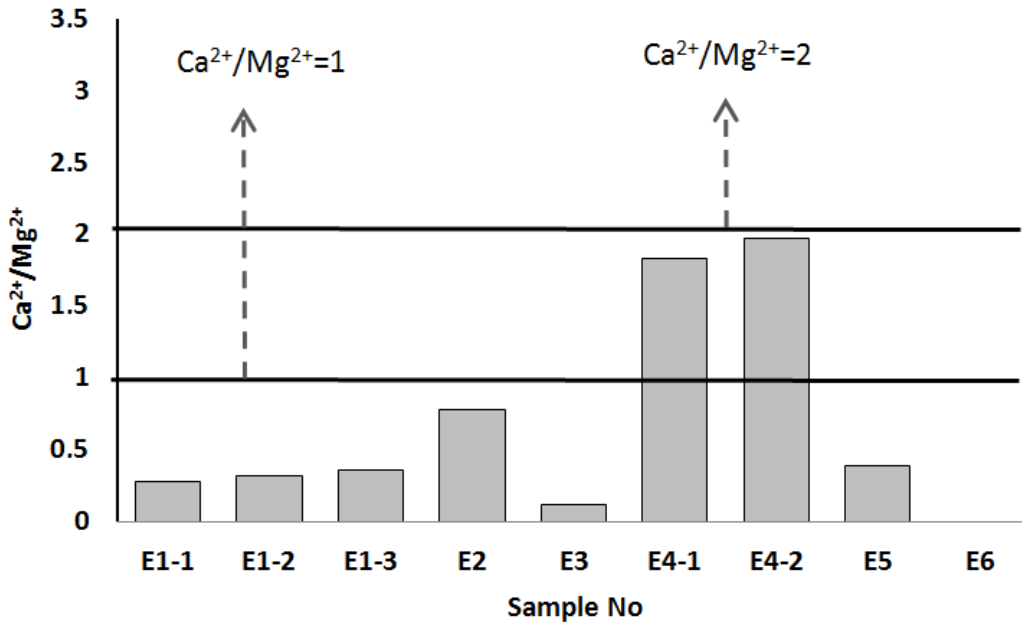
Figure 4. Ca^{2+}/Mg^{2+} molar ratio diagram.

Table 3. Isotope results of groundwater samples.

Parameters	E1-1	E1-2	E1-3	E2	E3	E4-1	E4-2	E5	E6
Sampling Date	18.1.2013	26.06.2013	18.9.2014	26.06.2013	26.06.2013	26.06.2013	18.9.2014	26.06.2013	18.9.2014
$\delta\ ^{18}O$	−6.12	n.d.	−5.71	−6.16	−5.69	−6.52	−6.18	−4.39	−4.26
$\delta\ ^{2}H$	−31.6	n.d.	−30.0	−33.2	−27.4	−32.4	−35.0	−24.3	−26.0
^{3}H	0.57	n.d.	n.d.	0.53	n.d.	3.46	n.d.	5.74	3.73

Table 4. Geochemical features of the dissolved gases. Data in ppm by vol. bdl = below detection limits; n.a. = not analyzed. Isotopic ratio of helium corrected for the atmospheric contamination R/Rac; (*) data after D'Alessandro et al., 2018. Site names and dates as in Table 1.

Site No	He ppm	H_2 ppm	O_2 ppm	N_2 ppm	CO ppm	CH_4 ppm	C_2H_6 ppm	CO_2 ppm	R/Ra	Rc/Ra	$^{4}He/^{20}Ne$	$d^{13}C_{CO2}$	$CO_2/^{3}He$
E1-1	12.0	5	476	11,300	0.10	15	–	958,300	2.60	2.60	61.1	N/A	2.21E+10
E1-2	10.0	5	199	7400	4.0	14	–	994,300	2.60	2.60	71.5	N/A	2.75E+10
E2	0.0	5	442	957	0	0	–	962,000	1.20	1.30	0.986	−2.2	1.33E+13
E4-1	246	2	322	577,500	0.80	996	–	397,100	2.82	2.85	23.9	−4.8	4.08E+08
E4-2	300	5	1500	504,800	0.90	1066	–	394,900	2.89	2.91	27.5	N/A	3.25E+08
E5	65.3	5	45,700	490,900	2.64	247	–	463,100	4.85	5.55	1.84	−2.7	9.19E+08
E6*	107	5	78	44,400	0	941,900	2883	100	3.14	3.20	12.4	N/A	2.10E+05
E6	126.1	43	122,400	675,000	1	202,200	–	265	–		n. d.	N/A	–

Cross-diagrams provide detailed information about ion sources in the groundwater. The plots of Figures 5a–5h highlight a close correlation between major ions (Cl, Na, K, Ca, Mg, and HCO_3) and TDS with the coefficients (R^2) in the range of 0.88–0.91 (Figures 5a–5h). Sample E-6 (Gökdere spring) which is underserpentinization process,

falls out of the correlation line due to very low bicarbonate contents, the absence of Mg, and the high amount of Na and Cl.

Samples falling on the total cations vs. $Ca^{2+} + Mg^{2+}$ 1:1 line (Figure 6) show that some of $Ca^{2+} + Mg^{2+}$ are sourced from the weathering of silicate minerals (Kumar et al.,
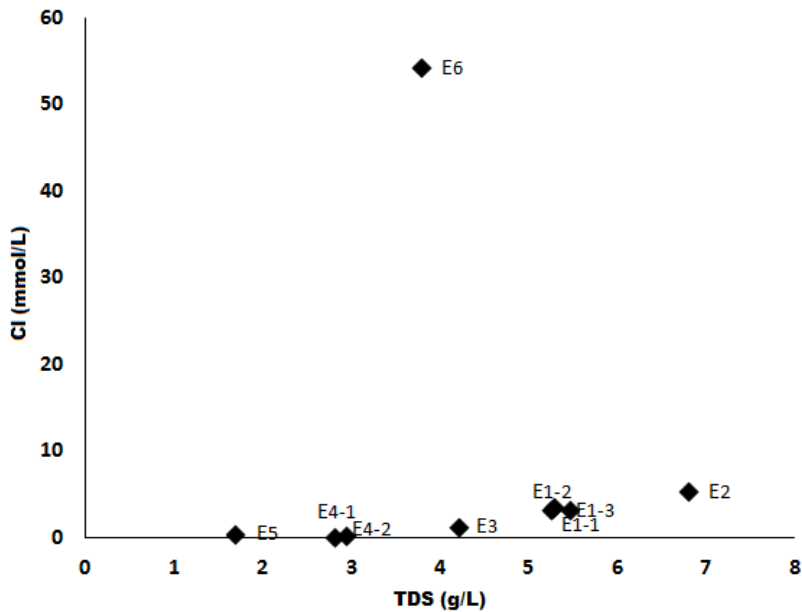
Figure 5a. TDS-Cl cross diagram.
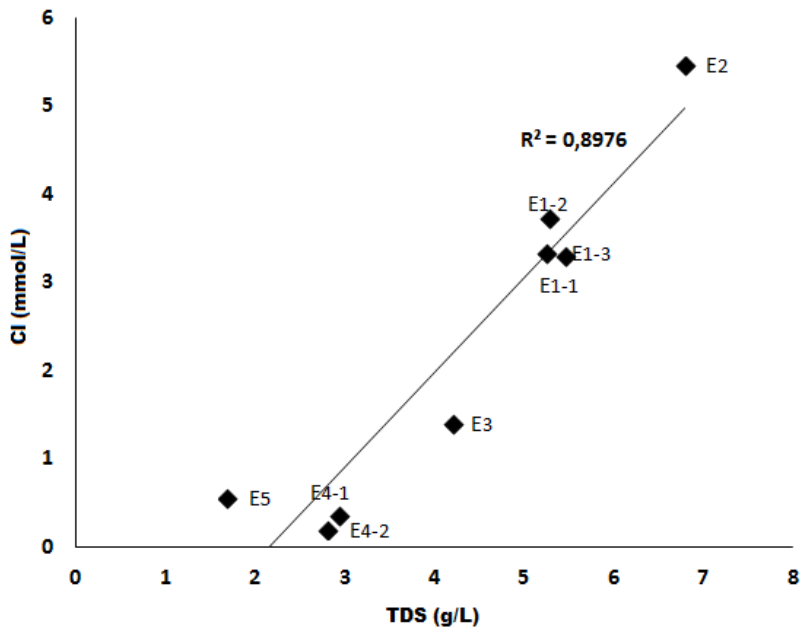
Figure 5b. TDS-Cl cross diagram.
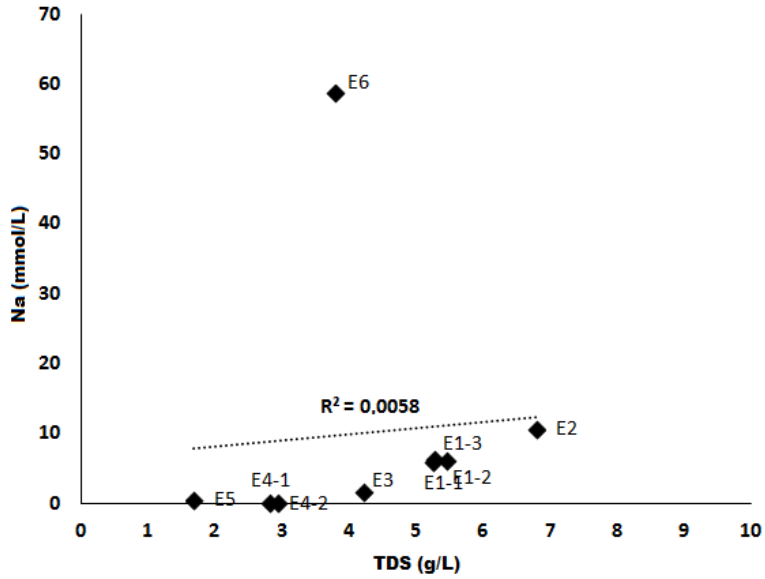
Figure 5c. TDS-Na cross diagram.
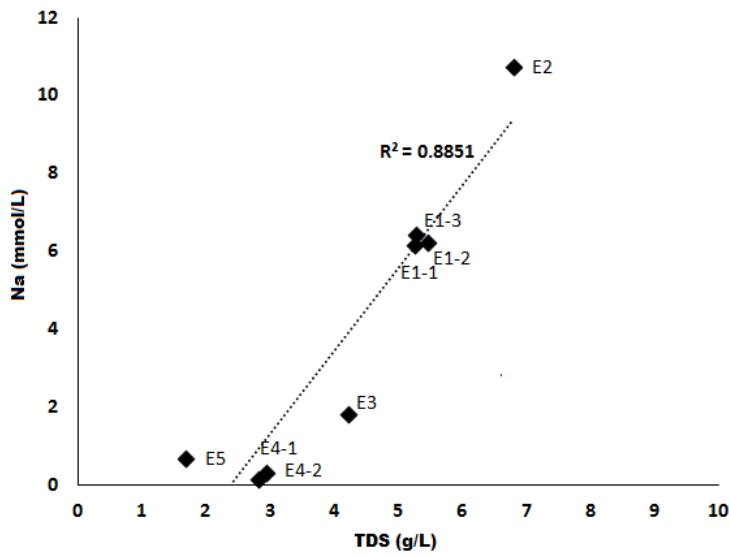
Figure 5d. TDS-Na cross diagram.

2009). As a matter of fact, either the Pleistocenic and the volcanic rocks of the Quaternary age can be the source of Ca and Mg for the sampled thermal waters, but sample E6 clearly represents groundwaters with a deep circulation in ophiolitic rocks (Cipolli et al., 2004; Yuce et al., 2014).

4.3. Isotopic composition of waters
The Global Meteoric Water Line (GMWL, Craig, 1961) and the Eastern Mediterranean Meteoric Water Line (EMMWL, Gat and Carmi, 1970) are shown in Figure 7, which indicates all water samples are of meteoric origin.

The influence of evaporation on groundwater chemistry is also ratified by the deviation of the $d^{18}O$ and d^2H values of groundwater samples from the Eastern Mediterranean Meteoric Water Line (EMMWL) (Figure 7). The groundwater samples that are plotted between the EMMWL and the GMWL can be separated into a few
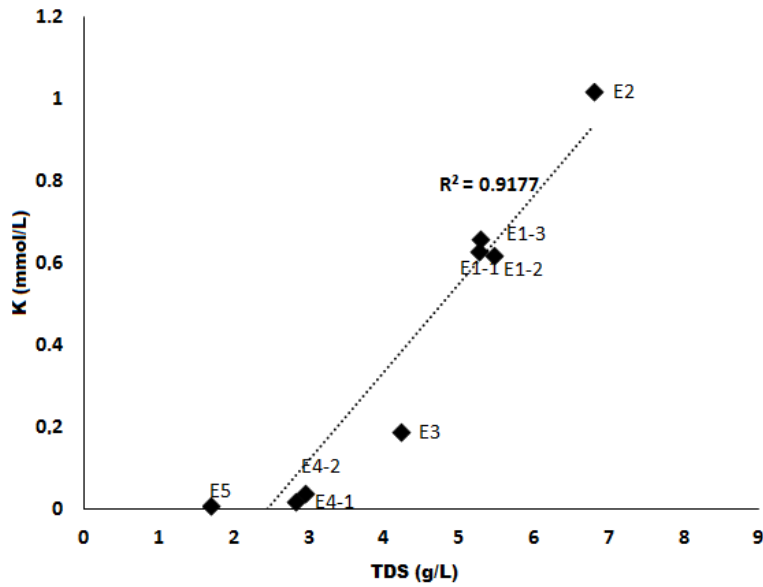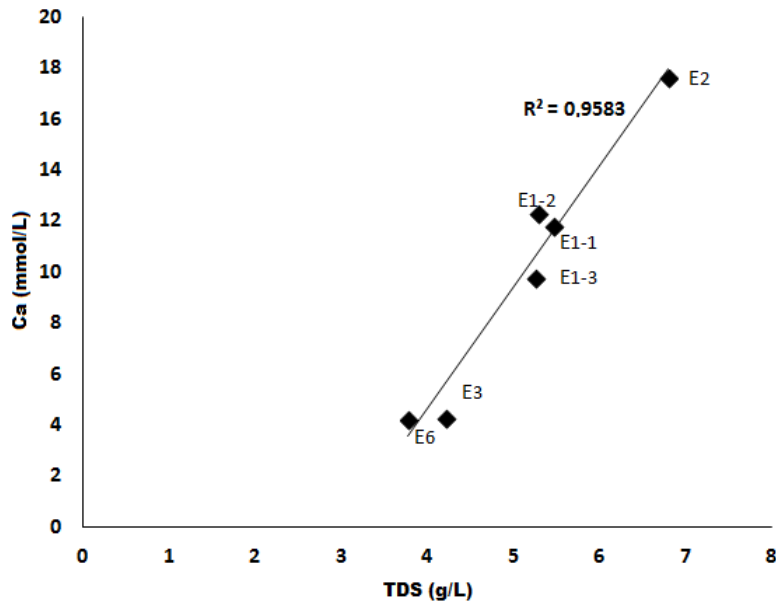
Figure 5e. TDS-K cross diagram.

Figure 5f. TDS-Ca cross diagram.

subgroups based on their positions. Subgroup I, located in the lower part of Figure 7 with more negative δD and δ^{18}O values, is representative of groundwater recharged by high-altitude precipitation while subgroup II, located upper part of Figure 7, was either composed of groundwater samples recharged by rainwater in a lower altitude area or was exposed to evaporation. However, since deep-circulated groundwater cannot undergo an evaporation process,

most probably related to the recharge from surface water or shallow groundwater that had been previously affected by evaporation.

As a matter of fact, the collected thermal waters, but the E6 sample, fall between the EMMWL and the GMWL accounting for a recharge from inland, Mediterranean-type precipitations. Furthermore, E5 and E6 samples are slightly shifted to the right due to oxygen-18 enrichment
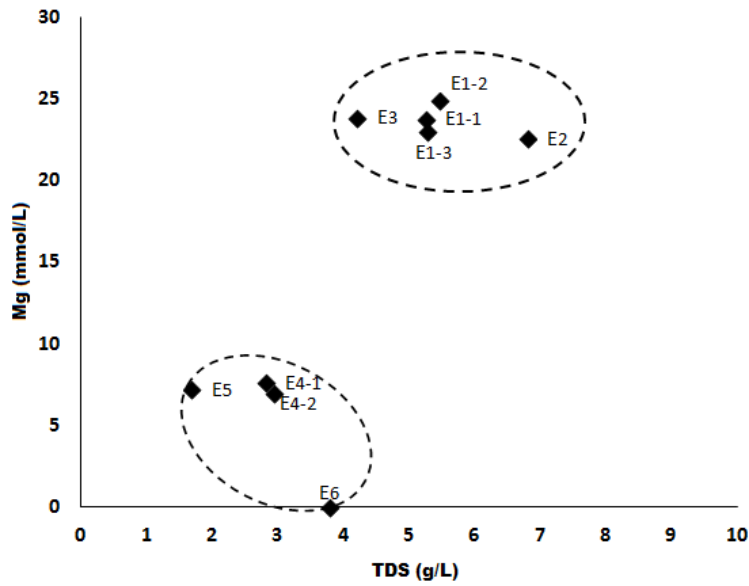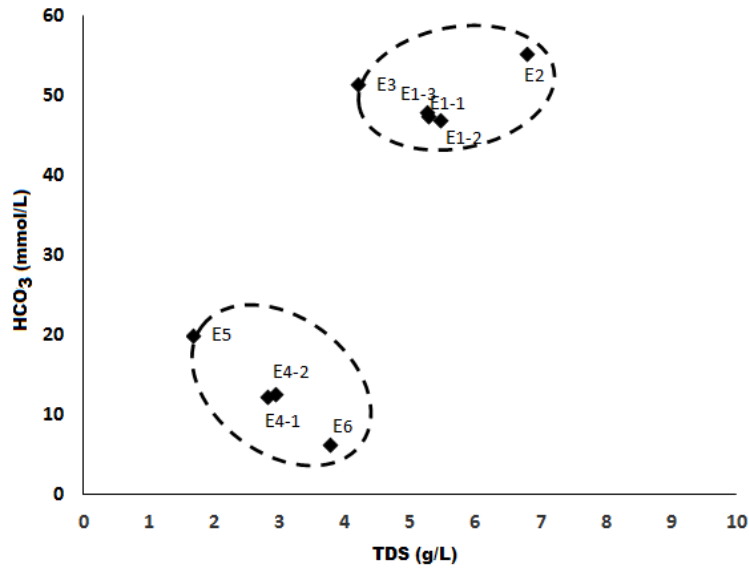
Figure 5g. TDS-Mg cross diagram.

Figure 5h. TDS-HCO$_3$ cross diagram.

as a result of water-rock interaction besides possible, although limited, evaporation effects.

Tritium is the radioactive isotope of hydrogen which has a half-life of 12.32 years, thus an ideal tracer in hydrological research to trace the time length of the water circulation. ^{3}H levels in the collected waters range from 0.53 to 5.74 TU (Table 4).

The Cl-tritium and Cl-^{18}dO graphs (Figure 8a, Figure 8b) are used to identify the relative circulation depth of groundwater. As a matter of fact, the higher chloride and lower tritium and depleted oxygen-18 values refer to relatively deep circulating groundwater, while lower chloride and higher tritium and enriched oxygen-18 values represent relatively shallow circulation of groundwater. As can be seen in Figure 8a and Figure 8b, samples E1-1 and E2 have relatively deep circulation.
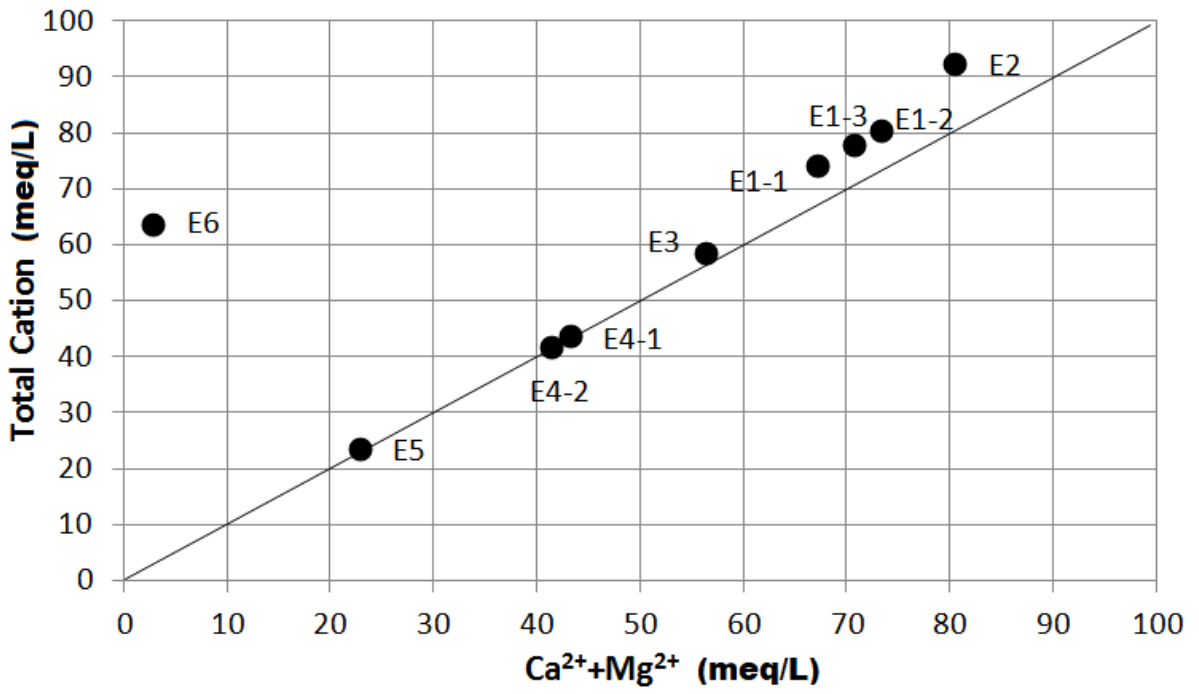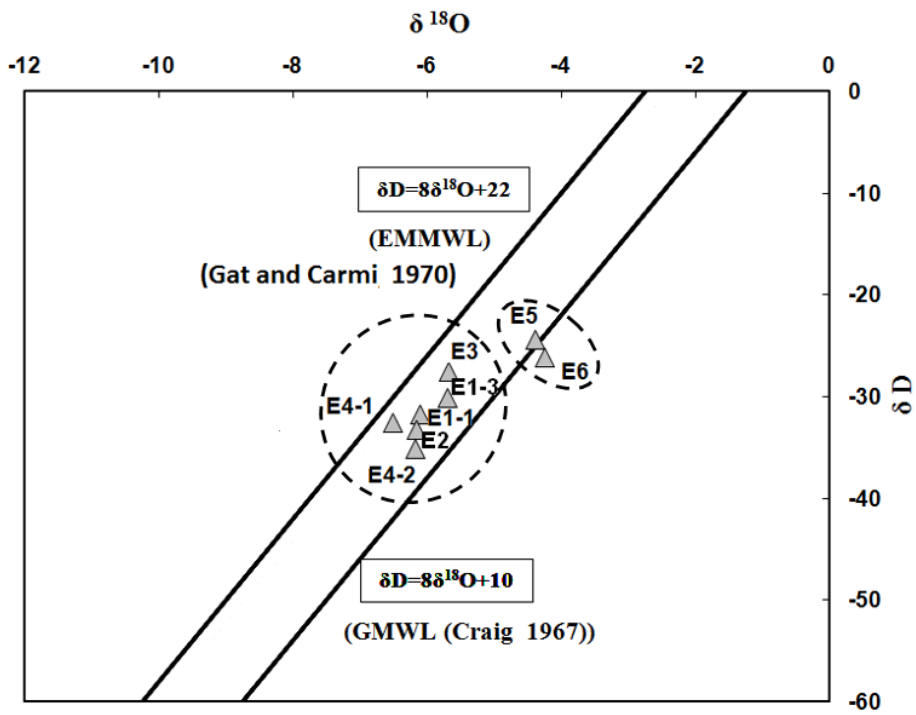
Figure 6. $Ca^{2+}+Mg^{2+}$vs. total cations.

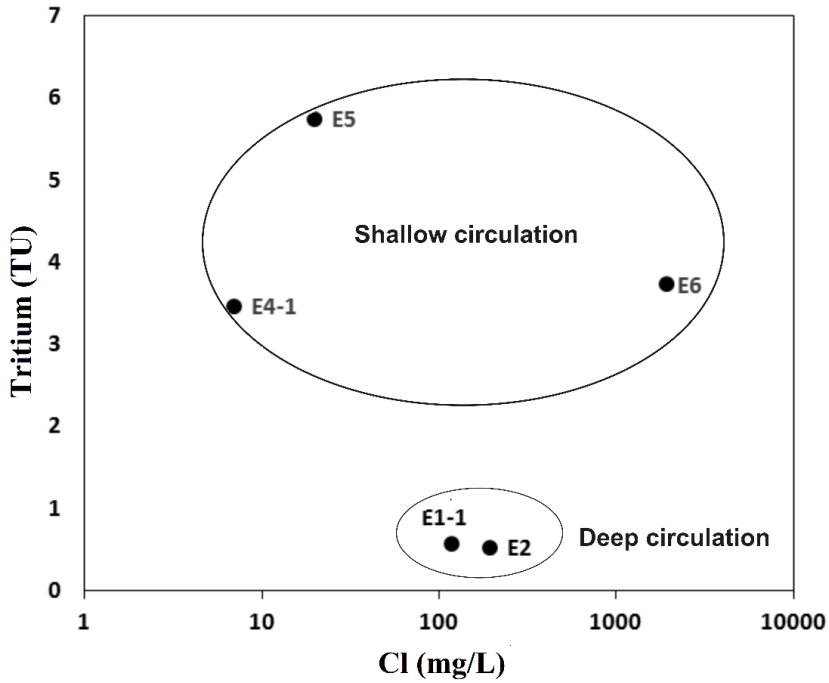**Figure 7.** ^{18}dO-dD diagram.
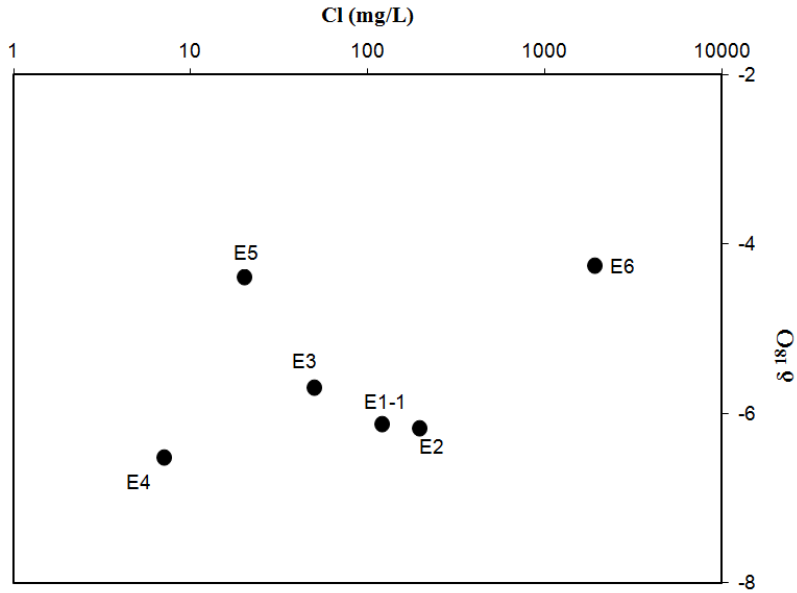
Figure 8a. Cl vs. ^{3}H diagram.

Figure 8b. Cl vs. ^{18}dO diagram.

4.4. Reservoir temperatures estimations

The temperature at 600 m depth was measured as 31.2 °C by MTA well in Erzin (TÜBİTAK 2015). Using the equation given above, the geothermal gradient was calculated as 21.5 °C /km (mean annual surface temperature was taken at 18.3 °C according to Turkish Meteorological Service). Thus, this result shows a slightly low-enthalpy area, however, it is deserved to make further geothermal explorations.

The chemical compositions of the water samples were plotted on the Na-K-Mg triangle diagram (Giggenbach 1991) to analyze their suitability as a geothermometer
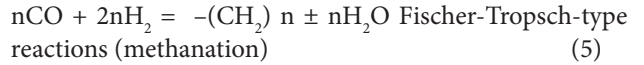
(Figure 9). The results show that all waters are immature waters, thus indicating the absence of equilibrium with the hosting rocks, with a possible equilibrium temperature of less than 60 °C. Sample E6 denotes a higher equilibrium temperature, in the range of 180 °C (Giggenbach, 1988).

The silica geothermometers (Table 4), based on the quartz and chalcedony solubility, were also used to estimate in an independent way the reservoir temperatures. The estimations provided coherent temperatures in the range of 58–162 °C (Table 5).
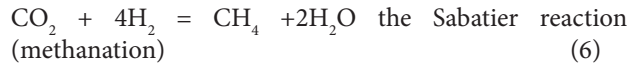
4.5. Gas geochemistry

The chemical composition of the dissolved gas phase highlights the interaction of a gas phase different from the atmosphere for all the sampling sites.

The presence of CO_2 (samples E1, E2) and CH_4 (sample E6) as dominant species in the dissolved gases testify that deep-originated components feed the sampled groundwaters. The nitrogen excess in E4 and E5 samples is associated with high CO_2 contents with the contemporary presence of significant helium concentrations that for sample E4 are the highest of the sample suite. The large CH_4 content of sample E6 is related to the serpentinization process of an ophiolitic block. CH_4 is produced by methanation following Fisher-Tropysh and Sabatier type reactions (D'Alessandro et al., 2018) which details are given below.

$$nCO + 2nH_2 = -(CH_2) n \pm nH_2O \text{ Fischer-Tropsch-type}$$
reactions (methanation) (5)
and
$$CO_2 + 4H_2 = CH_4 + 2H_2O \text{ the Sabatier reaction}$$
(methanation) (6)

The produced methane is purely abiogenic as shown by d^2D and $d^{13}C$ values of –7.9 ‰ and –137 ‰, respectively (D'Alessandro et al., 2018).

To trace the origin of the deep-originated gases, we used the helium isotope ratios that range from 1.3 to 5.55 times the atmospheric ratio. Figure 10 plots the samples on the triangular diagram ^3He-^4He-CO_2, showing that, although one sample (E1-1) is close to atmospheric end-member, both the CO_2-dominated samples and the CH_4-rich gas of sample E6 are ^3He enriched and fall on lines between 2.5Ra and MORB (Mean Oceanic Rift Basalt) value, i.e. 8Ra.

Figure 11 R/Ra vs $^4He/^{20}Ne$ provides a detail on the isotopic ratios of the sampled waters. The curves on the graph show different theoretical mixings between an atmospheric gas (R/Ra = 1 and $^4He/^{20}Ne = 0.318$) and mantle components characterized by end-members of 3.5Ra (from volcanic areas of central Italy); 5.5Ra assumed as representative of a deep mantle source of the study area and 6.5 Ra considered as representative of helium from European subcontinental mantle (Dunai and Baur, 1995).
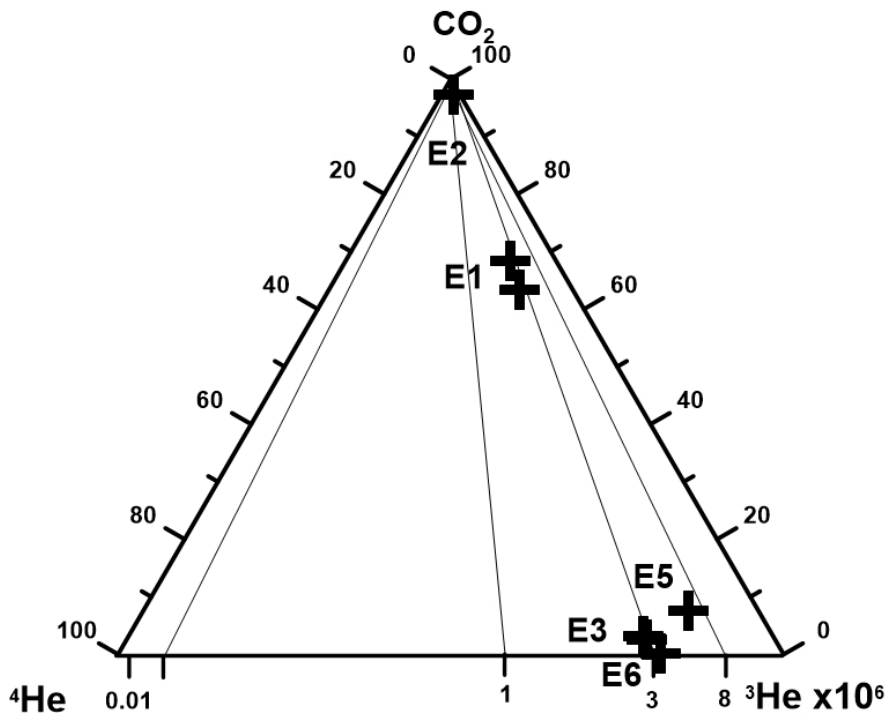

Figure 9. Giggenbach diagram.

Table 5. Estimated reservoir temperatures by silica geothermometers.

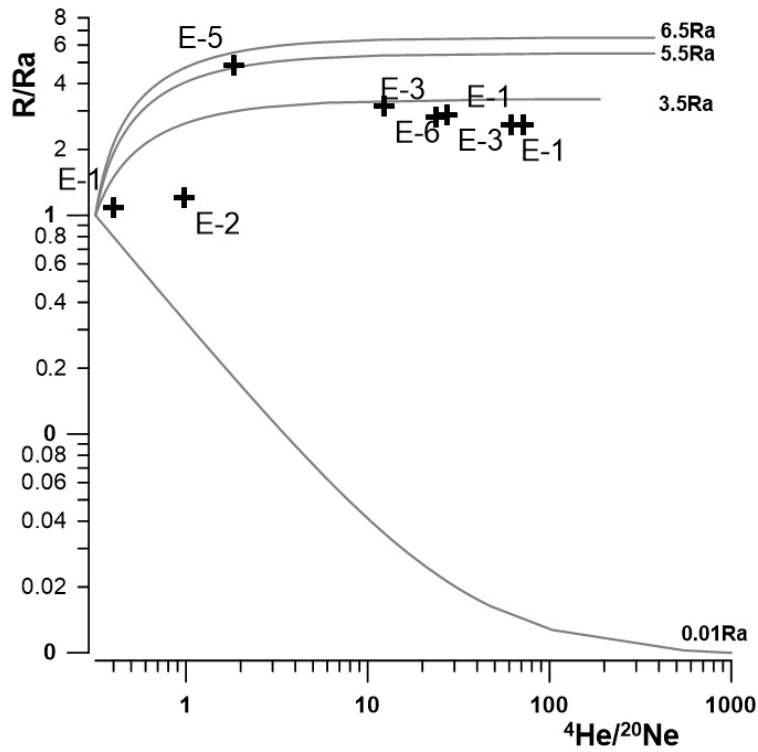| Sample No	Surface Temperature (°C)	SiO$_2$ mg/L	Quartz Estimated Temperature (°C)	Chalcedony Estimated Temperature (°C)	Chalcedony Estimated Temperature (°C)
Equation			T = 1309/(5.19–log SiO$_2$)–273.15	[1112/(4.91-logSiO$_2$)]-273.15	T = 1032/(4.69–log SiO$_2$) –273.15
Reference			(Fournier, 1977)	(Arnorsson et al., 1983)	(Fournier, 1977)
E1-1	27	144	159	130	134
E1-2	27.2	135	155	126	130
E1-3	27.2	141	157	129	133
E2	31.5	152.1	162	134	139
E3	22	118.4	147	118	121
E4-1	19.3	40.5	92	63	62
E4-2	19.6	37.7	89	60	58
E5	21.3	65.2	115	86	86

Figure 10. Ternary diagram of dissolved gases in water samples.

Finally, a mixing curve with a pure radiogenic helium source (R/Ra = 0.01) is shown. The dissolved helium in all the collected samples falls well above the atmospheric-type component also showing the absence of significant radiogenic contribution.

The significant contribution of mantle-derived helium is possibly due to the seismogenic deep seated active fault segments of the Düziçi-İskenderun Fault Zone (DIFZ). In fact, the highest ^{3}He content is recorded for sample E6, located over the extension of the Erzin Active Fault, and for sample E5 which is close to the Düziçi-İskenderun Active Fault Zone.
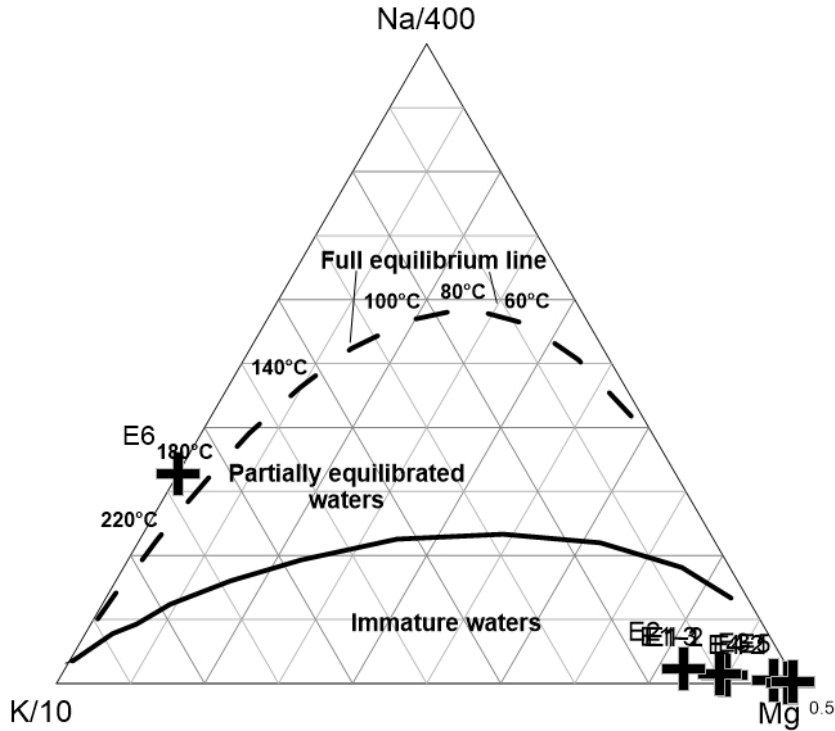
Figure 11. Diagram of R/Ra vs. ^{4}He/^{20}Ne.

4.6 The role of the active faults

Duman et al. 2020 during their paleoseismological field study, opened several trenches along the Sürgü-Misis Active Fault System including the DIFZ, segment. One of the trench (T7 in Figure 1) was opened at the northeast margin of the segment and the E5 gas sampling point is located in the southeast section of the segment. The distance of sampling point E5 to the trench no: T7 along the fault segment is ca. 5.5 km. Three surface faulting events were observed in the trench based on structural and stratigraphic relationships. The trench results confirm that there were three earthquakes that occurred between the 14th century BC and the 5th century AD. Although the trench area is located slightly beyond the study area, it is still a very consistent and promising observation that demonstrates the importance of active fault-gas relationships.

It is a very remarkable point to recognize such measurements are well consistent with each other. Our results for R/Ra had been measured in 2013–2014 while their study was realized by 2018–2019. By chance, I read it and contacted these researchers (i.e. authors of the paper) who are working for MTA (GD of Mineral Research and Exploration, Turkey). Therefore, the area seems to be very promising in terms of geothermal potential and is located in the active segments of DIFZ and TFS (Figure 1) (Duman et al., 2020).

The very low silica content of hyperalkaline waters (Table 2) with a saturation index well below quartz is characteristic of the unique mineral assemblage of ophiolitic rocks in their aquifers.

5. Conclusions

The analytical results of collected thermal waters displayed variable geochemical features as a function of the WRI and the dissolved gases. The saturation indices show that all groundwater are E1-1, E1-2, E1-3, and E6 are oversaturated with respect to aragonite, and most samples are slightly oversaturated with respect to calcite and dolomite. The ions dissolved in almost all the samples highlight interactions with either carbonatic and magmatic rocks. Sample E6, showing the highest pH of 11.4 and a large depletion in Mg content, is representative of serpentinization process indicating deep circulating in ophiolitic rocks. The δ^{18}O and δ^2H isotope composition of the groundwaters points out two subgroups relatively low and high stable isotope values and all waters are from the meteoric origin. Estimations of the reservoir temperatures provide equilibrium temperatures between 58 °C and 162 °C. Moreover, the significant mantle helium contribution denotes the upraising of deep volatiles that have been dissolved in the deep geothermal reservoir. The thermalism of the collected waters can be generated either

by circulation at deep levels and fast upraising favored by the faulted systems or high-temperature water rock exchanges with buried volcanic rock. The mantle helium contributions in the study area changes between 15% and 83% (Figure 1). The evidence that E5 sample, located in close vicinity to the trench number 7 (Duman et al., 2002) displays a very high helium isotopic ratio (5.55Ra) provides a clear indication of the possible role of the thermal waters as indicators of changes in the faulting activity. Therefore, we conclude that further detailed geothermal studies and new investigations on the relationships between temporal changes of the geochemical features and the seismic activity are highly recommended for this particular study area.

References

Agyemang VO (2020) Hydrochemical Characterization and Assessment of Groundwater Suitability for Drinking, Domestic and Irrigation Purposes in The Agona East District, Ghana. Iconic Research and Engineering Journals 3 (7): 112-125 ISSN: 2456-8880.

Altunel E, Meghraoui M, Karabacak V, Akyuz SH, Ferry M et al. (2009) Archaeological sites (Tell and Road) offset by the Dead Sea Fault in the Amik Basin, Southern Turkey. Geophysical Journal International 179: 1313-1329.

Arnorsson S, Gunnlaugsson E, Svavarsson H (1983) The chemistry of geothermal waters in Iceland-II. Mineral equilibria and independent variables controlling water compositions. Geochimica et Cosmochimica Acta 47: 547-566.

Cipolli F, Gambardella B, Marini L, Ottonello G, Zuccolini MV (2004) Geochemistry of high-pH waters from serpentinites of the Gruppo di Voltri (Genova, Italy) and reaction path modeling of CO_2 sequestration in serpentinite aquifers. Applied Geochemistry 19: 787–802.

Craig H (1961) Isotopic Variations in Meteoric Waters. Science 133: 1702-1703.

D'Alessandro W, Yuce G, Italiano F, Bellomo S, Gülbay AH et al. (2018) Large compositional differences in the gases released from the Kizildag ophiolitic body (Turkey): Evidence of prevailingly abiogenic origin. Marine and Petroleum Geology 89: 174-184.

Dewey JF, Pitman WC, Ryan WBF, Bonnin J (1973) Plate tectonics and the evolution of the Alpine system. Bulletin Geologic Society of America 84: 3137-3180.

Dilek Y, Thy P (2009) Island arc tholeiite to boninitic melt evolution of the Cretaceous Kizildag (Turkey) ophiolite: model for multi-stage early arc-forearc magmatism in Tethyan subduction factories. Lithos 113: 68–87.

Duman TY, Elmacı H, Özalp S, Kürçer A, Kara M et al. (2020) Paleoseismology of the western Sürgü–Misis Fault System: East Anatolian Fault, Turkey. Mediterranean Geoscience Reviews 2 (3): 411-437.

Dunai T, Baur H (1995) Helium, neon and argon systematics of European subcontinental mantle: Implication for its geochemical evolution. Geochimica et Cosmochimica Acta 59: 2767.

Fournier RO (1977) Chemical geothermometers and mixing models for geothermalsystems. Geothermics 5:41–50.

Gat JR. Carmi I (1970) Evolution of the isotopic composition of atmospheric waters in the Mediterranean Sea area. Journal of Geophysical Research 75: 3039–3048.

Giggenbach WF (1988) Geothermal solute equilibria: Derivation of Na- K-Ca-Mg geoindicators. Geochimica et Cosmochimica Acta 52:2749–2765.

Giggenbach WF (1991) Collection and analysis of geothermal and volcanic water and gas discharge, in application of geochemistry in geothermal reservoir development. (edited by F. D' Amore) Unitar, Rome 119-144.

Italiano F, Bonfanti P, Ditta M, Petrini R, Slejko F (2009) Helium and carbon isotopes in the dissolved gases of Friuli region (NE Italy): geochemical evidence of CO2 production and degassing over a seismically active area. Chemical Geology 266: 76–85.

Italiano F, Yuce G, Uysal IT, Gasparon M, Morelli G (2014) Insights into mantle-type volatiles contribution from dissolved gases in artesian waters of the Great Artesian Basin, Australia. Chemical Geology 378-379: 75–88.

Italiano F, Yuce G, Di Bella M, Rojay B, Sabatino G et al. (2017) Noble gases and rock geochemistry of alkaline intraplate volcanics from the Amik and Ceyhan-Osmaniye areas, SE Turkey. Chemical Geology 469: 34 46.

Karabacak V (2007) Ölü Deniz Fay Zonu Kuzey Kesiminin Kuvaterner Aktivitesi. Eskişehir Osmangazi Üniversitesi, Fen Bilimleri Enstitüsü, Doktora tezi, 286 (in Turkish).

Karabacak V, Altunel E, Meghraoui M, Akyüz HS (2010) Field evidences from northern Dead Sea Fault Zone (South Turkey): New findings for the initiation age and slip rate. Tectonophysics 480: 172–182.

Katz BG, Davis JH, Coplen TB, Bullen TD (1997) Use of chemical and isotopic tracers to characterize the interactions between ground water and surface water in mantled karst. Ground Water 35:1014–1028.

Kumar SK, Rammohan V, Sahayam JD, Jeevanandam M (2009) Assessment of groundwater quality and hydrogeochemistry of Manimuktha River basin, Tamil Nadu, India. Environmental Monitoring and Assessment 159: 341.

Lakshmanan E, Kannan K, Senthil KM (2003) Major ion chemistry and identification of hydrogeochemical process of groundwater in part of Kancheepuram district, Tamilnadu, India. Journal of Environmental Geosciences 10 (4): 157–166.

Li PY, Wu JH, Qian H (2012) Assessment of groundwater quality for irrigation purposes and identification of hydrogeochemical evolution mechanisms in Pengyang County, China. Environmental Earth Science 69: 2211–2225.

Mahmoudi N, Nakhaei M, Porhemmat J (2017) Assessment of hydrogeochemistry and contamination of Varamin deep aquifer, Tehran Province, Iran. Environmental Earth Science 76: 370

Marghade D, Malpe DB, Zade AB (2012) Major ion chemistry of shallow groundwater of a fast growing city of Central India. Environmental Monitoring and Assessment 184: 2405–2418.

Mayo AL, Loucks MD (1995) Solute and isotopic geochemistry and groundwater flow in the Central Wasatch Range, Utah. Journal of Hydrology 172: 31-59.

Mezga K, Urbanc J (2014) Groundwater calcium and magnesium content in various lithological types of aquifers in Slovenia L. Razowska-Jaworek (Ed.), Calcium and Magnesium in Groundwater Occurrence and Significance for Human Health. Taylor & Francis Group, London.

Nagaraju A, Suresh S, Killham K, Hudson-Edwards K (2006) Hydrogeochemistry of waters of Mangampeta a barite mining area, Cuddapah basin, Andhra Pradesh, India. Turkish Journal of Environmental Science 30: 203–219.

Narany TS, Ramli MF, Aris AZ, Sulaiman WNA, Juahir WH et al. (2014) Identification of the hydrochemical processes in groundwater using classic integrated geochemical methods and geostatistical techniques in Amol-Babol Plain, Iran. The Scientific World Journal.

Özyurt NN, Bayarı CS, Doğdu MŞ, Arıkan A (2001). Akkuyu körfezi (Mersin) deniz suyunun fiziksel ve kimyasal özelliklerini etkileyen süreçler, Yerbilimleri 24: 113-126 (in Turkish).

Perinçek D, Çemen İ (1990) The structural relationship between the East Anatolian and Dead Sea fault zones in southeastern Turkey. Tectonophysics 172: 331-340.

Rojay B, Heimann A, Toprak V (2001) Neotectonic and volcanic characteristics of the Karasu fault zone (Anatolia, Turkey): The transistion zone between the Dead Sea transform and the East Anatolian fault zone. Geodinamica Acta 14: 197-212.

Sano Y, Wakita H (1988) Precise measurement of helium isotopes in terrestrial gases. Bulletin of the Chemical Society of Japan 61 (4): 1153-1157.

Schoeller H (1977) Geochemistry of groundwater. In: Groundwater Studies an International Guide for Research and Practice. UNESCO, Paris 15: 1–18.

Setiawan T, Alam BYS, Haryono E (2020) Hydrochemical and environmental isotopes analysis for characterizing a complex karst hydrogeological system of Watuputih area, Rembang, Central Java. Indonesia. Hydrogeology Journal 28: 1635–165.

Şener F, Şener M, Yiğit B (2021) Geochemical proxies and formation mechanism of Hatay (Başlamış) travertine and relation with Dead Sea Fault Zone (S-Turkey). Journal of African Earth Sciences 177: 104126.

Şengör AMC, Yilmaz Y (1981) Tethyan evolution of Turkey: A plate tectonic approach. Tectonophysics 75: 181–241.

Tatar O, Piper JDA, Gürsoy H, Heimann A, Koçbulut F (2004) Neotectonic deformation in the transition zone between the Dead Sea Transform and the East Anatolian Fault Zone, Southern Turkey: a paleomagnetic study of the Karasu Rift Volcanism. Tectonophysics 385: 17–43.

Thakur T, Rishi MS, Pradeep K, Naik PK, Sharma P (2016) Elucidating hydrochemical properties of groundwater for drinking and agriculture in parts of Punjab, India. Environmental Earth Sciences 75: 467.

TUBITAK (2015) Determination of Fault Activity and Geothermal Origin by Soil and Groundwater Degassing: The Extension of Dead Sea Fault Zone (DSFZ) in the Amik Basin (Hatay) and its Relation with Karasu Fault Zone and Origin of Thermal Waters in Amik Basin. TUBITAK-cost Research Project in the Frame of COST Action Project No: 111Y090, Project Final Report, June 2015 p. 215 (in Turkish).

Wigley TML (1977) WATSPEC: A computer program for determining the equilibrium speciation of aqueous solutions. Norwich:Geo-Abstracts for the British Geomorphological Research Group 20: 48.

Yuce G, Italiano F, D'Alessandro W, Yalcin TH, Yasin DU et al. (2014) Origin and interactions of fluids circulating over the Amik Basin (Hatay, Turkey) and relationships with the hydrologic, geologic and tectonic settings. Chemical Geology 388: 23-39.

Yuce G, Fu CC, D'Alessandro W, Gulbay AH, Lai CW et al. (2017) Geochemical characteristics of soil radon and carbon dioxide within the Dead Sea Fault and Karasu Fault in the Amik Basin (Hatay), Turkey. Chemical Geology 469: 129–146.